11,08,12

Resistive gas sensors based on a polyene-polyyne structure with embedded TiO_2 nanoparticles

© I.F. Nuriahmetov, O.A. Streletskiy, A.V. Pavlikov, N.F. Savchenko, A.A. Tatarintsev, A.A. Khaidarov

Moscow State University,
Moscow, Russia

E-mail: islam.nuriakhmetov@mail.ru

Received November 11, 2025
Revised November 28, 2025
Accepted December 4, 2025

The paper presents the results of studies of gas sensors based on a polyene-polyyne structure with embedded TiO_2 nanoparticles. The samples were prepared by dissolving polyvinylidene fluoride in N,N-dimethylformamide followed by its dehydrohalogenation at different concentrations of TiO_2 nanoparticles. The structure of the samples was studied using scanning electron microscopy, energy-dispersive X-ray spectroscopy, Raman spectroscopy, and infrared Fourier transform spectroscopy. The research results show that the obtained samples are porous films based on polyene-polyyne chains, in the matrix of which TiO_2 nanoparticles are located. Studies of the sensory properties of the manufactured samples were carried out for various concentrations of ethanol, acetone, and ammonium hydroxide vapors. The samples showed a general increase in sensitivity to all the gases studied with an increase in the concentration of TiO_2 nanoparticles. With an increase in the mass fraction of TiO_2 nanoparticles, an optimal value was observed, at which the sensitivity to ammonium hydroxide vapors became maximum.

Keywords: Polyene-polyyne chains, dehydrohalogenation, TiO_2 nanoparticles, composites, selective resistive sensing, porous sp-based films.

DOI: 10.61011/PSS.2025.12.63086.320-25

1. Introduction

The development of reliable and highly sensitive gas sensors is an urgent task for creating effective sensors for monitoring toxic, explosive and flammable gases that are used in various industries, in agriculture, in the pharmaceutical and food industries.

As a rule, only specific gases such as methane, ammonia, oxygen, carbon dioxide and carbon monoxide require control of the concentration of gases in the atmosphere in production, which allows the use of relatively cheap sensors that measure infrared (IR) radiation, changes in thermal conductivity, electrical resistance, etc. Resistive gas sensors are of particular interest due to their low cost, ease of manufacture, high stability, and sensitivity [1]. The disadvantages of this type of sensor include low selectivity and relatively high operating temperature. These problems can be resolved by using new types of materials, such as modified carbon materials [2].

Determination of the ammonia content in the atmosphere is an important task, since ammonia is a toxic substance and heavily pollutes the environment [3]. Disruptions in technological processes that produce ammonia vapors pose a significant threat to both human health and nature, so the development of new, reliable methods for controlling ammonia concentrations is a top priority for both science and industry.

A method was proposed in Refs. [4,5] for obtaining carbon material based on dehydrofluorinated polyvinylidene fluoride (d-PVDF), which showed high values in sensory response, to create highly sensitive resistive gas sensors. The synthesis of carbon material by dehydrohalogenation of the precursor leads to the formation of pores and chemically active sites [6] forms a structure based on *sp*-hybridized carbon atoms, which ensures its high sensory characteristics.

Carbon materials obtained were defined as „polyene-polyyne“ in Refs. [4,7], which indicates a chain structure consisting of both *sp*-hybridized (polyyne) and sp^2-hybridized (polyene) linear fragments. The materials are also of particular interest for various applications due to a number of properties: the relationship between the length of the linear fragment and the band gap [8], high thermal conductivity and high mechanical strength [9], spin-polarized electron transfer [10], ballistic [11] and tunnel [12] conduction.

Assuming that the carbon material based on d-PVDF has a high selectivity for vapors containing ammonia [4], and that nanoparticles based on TiO_2 have a good sensory response to ammonia [13], an attempt is made in this study to modify a material based on films of dehydrohalogenated PVDF with TiO_2 nanoparticles in various concentrations in order to optimize its properties, increase sensitivity and selectivity.

The modified material was studied, its structure was examined by scanning electron microscopy, energy-dispersive X-ray spectroscopy, Raman spectroscopy, and Fourier transform IR spectroscopy, and gas-sensitive properties were measured with respect to ethanol, acetone, and ammonium hydroxide vapors.

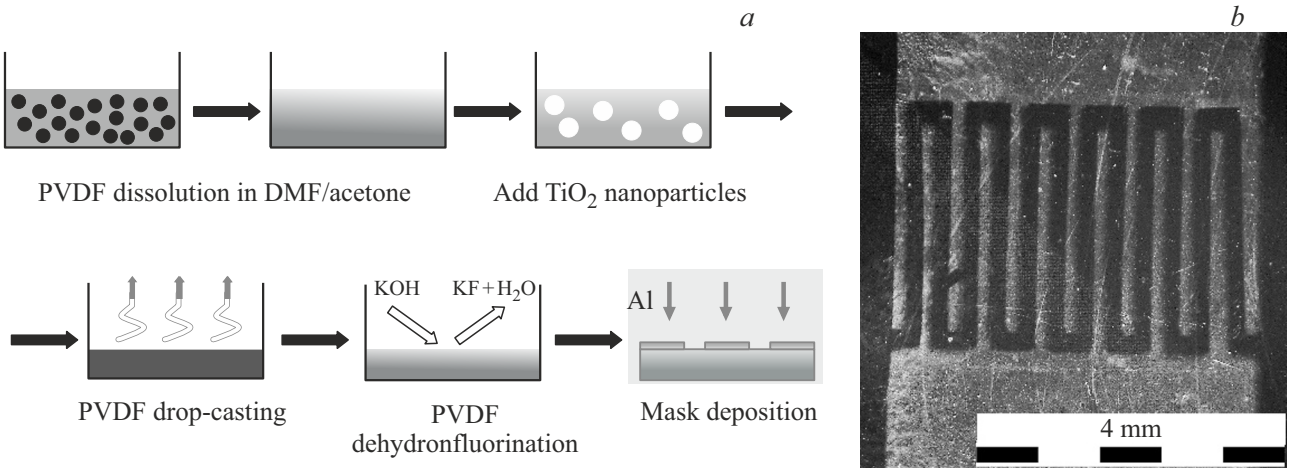

Figure 1. *a*) Sensor manufacturing scheme, *b*) film with sputtered contacts.

2. Methodology and materials

2.1. Preparation of the material

The sample preparation process takes place in several stages (Figure 1, *a*). PVDF powder is used as a precursor (LLC „KhimMed", Moscow, Russia). At the first stage, 100 mg of PVDF powder is dissolved in 25 ml of a mixture of N,N-dimethylformamide (DMF) (LLC „Ruskhim", Moscow, Russia) and acetone (LLC „KhimMed", Moscow, Russia) in a ratio of 7,:3 at a temperature of 60 °C. A nanodisperse powder of TiO_2 particles (Sigma-Aldrich company) is added to the resulting solution in an amount of 0.5, 1.0, 5.0 mg for different samples. The average particle size is 30 nm. Then the solution is poured into a glass Petri dish with a diameter of 9 cm (LLC „MLS Klin", Moscow, Russia) and dried until the solvent has completely evaporated. After drying, a thin film of the finished material forms at the bottom of the Petri dish. Thin translucent PVDF films with different mass fractions of nanoparticles TiO_2 were obtained by this method. The thickness of the finished film was about 1 μm. In the future, the name of the samples will be written as follows: PVDF-TiO_2.

A chemical dehydrofluorination reaction of PVDF-TiO_2 films was performed at room temperature at the second stage of sample production. A solution of potassium hydroxide KOH (LLC „LABTECH", Moscow, Russia) in methanol CH_3OH (LLC „LABTECH", Moscow, Russia) was prepared for this the reaction. For this purpose, KOH crystals were dissolved in methanol until a supersaturated solution was formed. Next, acetone CH_3COCH_3 was added to the resulting solution in a ratio of 1 : 9, with a thorough mixing. Then PVDF-TiO_2 films were completely immersed in the KOH-CH_3OH-CH_3COCH_3 solution.

The interaction of KOH and PVDF-TiO_2 resulted in a dehydrohalogenation reaction [14]:

$$(n+m)(-CH_2-CF_2-)+2(n+m)KOH \rightarrow (-CH{=}CF-)_n + (-C{\equiv}C-)_m + 2(n+m)H_2O + 2(n+m)KF.$$

The reaction took place at room temperature for 24 hours. As a result of the reaction, the appearance of the film changed from translucent to opaque black.

Subsequently, residual products were removed from the obtained samples by rinsing them in an ultrasonic bath (Wahluen Electronic Tools Corporation, Shantou, China) filled with distilled water for 15 minutes. The film was dried after ultrasonic cleaning and 5×5 mm samples were prepared. Four samples with different mass fractions of nanoparticles TiO_2 were obtained: d-PVDF (dehydrohalogenated PVDF film without the addition of nanoparticles TiO_2), d-PVDF-TiO_2-0.5 (dehydrohalogenated PVDF film with addition of 0.5 % of the mass of PVDF nanoparticles TiO_2), d-PVDF-TiO_2-1.0 (dehydrohalogenated PVDF film with 1.0 % of the mass of TiO_2), d-PVDF-TiO_2-5.0 (dehydrohalogenated PVDF film with 5.0 % of TiO_2).

At the third stage, aluminum metal contacts were deposited on the surface of the samples using magnetron deposition. Special titanium masks were placed on top of the samples to shade the sensor's working area. The samples with masks were placed in a high vacuum chamber, followed by pumping to pressure $1.3 \cdot 10^{-3}$ Pa. Next, argon gas was injected into the working chamber to a pressure of $1 \cdot 10^{-2}$ Pa, and the process of magnetron deposition of the aluminum coating began. Aluminum films were deposited using a high-frequency magnetron source (13.56 MHz) with an operating power of 100 W. The thickness of the deposited coating was monitored using a quartz thickness sensor (Inficon Corporation, Moscow, Russia). Figure 1, *b* shows an image of a carbon film with sprayed contacts. The width of the working surface is 0.2 mm, and the total length is 39 mm.

2.2. Research of the material

The surface of the samples was examined using a LEO 1455 VP scanning electron microscope (Carl Zeiss, Jena, Germany). The accelerating voltage was 10 kV. Secondary

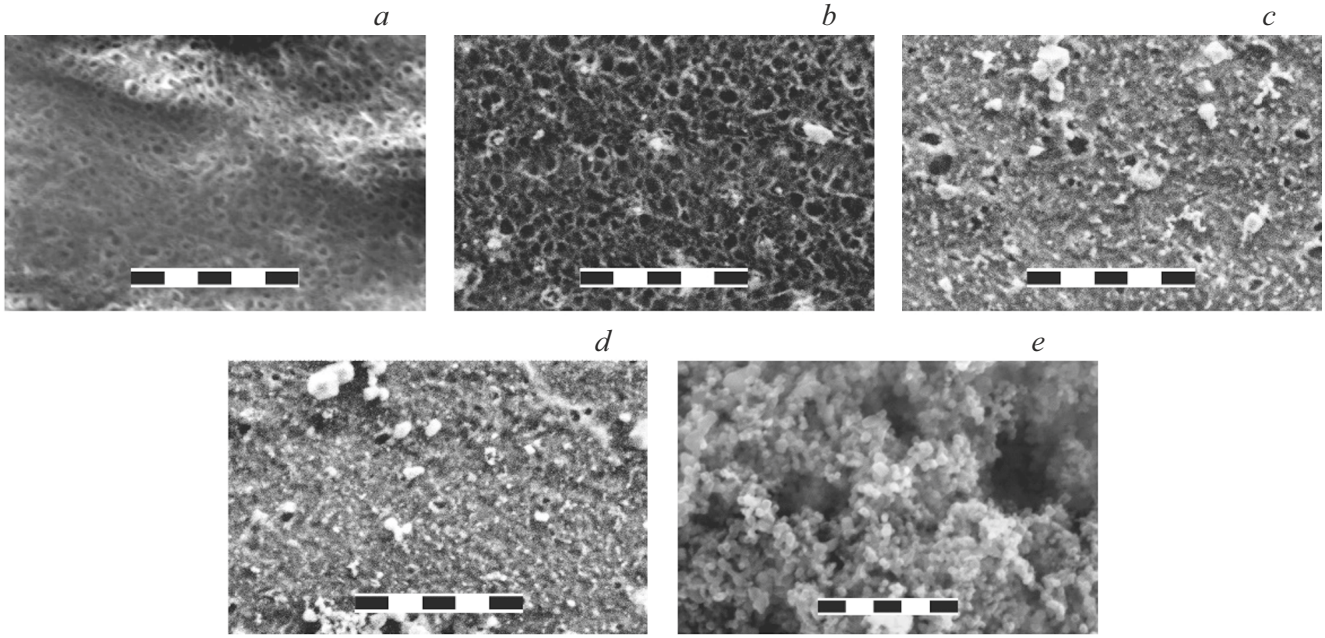

Figure 2. *a*) SEM images of d-PVDF, *b*) d-PVDF-TiO_2-0.5, *c*) d-PVDF-TiO_2-1.0, *d*) d-PVDF-TiO_2-5.0, *e*) TiO_2. The size of the scale marker is 1 μm (*a*–*d*), 500 nm (*e*).

electrons were recorded using the Everhart–Thornley detector. Scanning electron microscopy (SEM) results were processed using Gwyddion software to determine surface concentrations and average pore sizes and particle sizes.

Raman spectroscopy of light was performed using a Sunshine GE-Raman spectrometer (Changchun New Industries Optoelectronics Tech (CNI) company, Changchun, China) coupled with a Leitz Wetzlar metallographic microscope (Ernst Leitz Corporation, Wetzlar, Germany). The exciting wavelength was 532 nm, power 1 mW, resolution 6 cm^{-1}. A series of changes were performed from 3–5 areas on the surface for each sample. The most characteristic spectra were selected for illustration in the graphs below. The scan results were processed in the MagicPlot software package.

IR spectroscopy was performed using a Brucker IFS-66v/S FTIR spectrometer (Bruker Optics, Karlsruhe, Germany). The resolution of the IR spectrometer was 4 cm^{-1}.

X-ray diffraction analysis was performed using a Rigaku D/MAX-2500 diffractometer with radiation CuK_α in the range from 10 to 60°.

2.3. Measuring sensory response

The sensory properties were measured on an installation located in a glove box (Plas-Labs, Lansing, USA). The samples were installed in a glove box and connected to a B5-50 power supply unit (RIAP plant, Nizhny Novgorod, Russia) and a nanoammeter paired with a Tektronix DMM4050 computer (National Instruments Corporation, Beverton, USA). The measurements were performed at room temperature. The relative sensory response $\Delta\sigma/\sigma_0$ was estimated using the equation

$$\frac{\Delta\sigma}{\sigma_0} = \frac{\sigma - \sigma_0}{\sigma_0}, \quad (1)$$

where σ_0 — the conductivity of the sample in ambient conditions, σ — the maximum conductivity of the sample when interacting with the detected gas, $\Delta\sigma$ — sensory response.

The duration of the reaction time was estimated as the time required to change the electrical conductivity from σ_0 to $\sigma_0 - 0.9\Delta\sigma$. The duration of the sensor relaxation time was estimated as the time required for a change in conductivity from σ to $\sigma + 0.9\Delta\sigma$.

3. Results

3.1. Scanning electron microscopy

Figure 2 shows images of samples obtained in SEM. Morphological features of the surface of the sample obtained without the addition of TiO_2 nanoparticles are manifested in the form of pores with characteristic sizes from 18 to 86 nm and a surface concentration of 62.3 μm^{-1}. Addition of nanoparticles TiO_2 with a mass fraction 0.5 % leads to an increase in pore size, and some of them begin to fill with nanoparticles. Apparently, the nanoparticles TiO_2 stimulate the formation of pores with large sizes in the range from 24 to 118 nm. The surface concentration of the nanoparticles TiO_2 is 8.46 μm^{-2}, and the average distance between them is 344 nm. The pore surface concentration is 68.4 μm^{-1}.

The free pores are filled with nanoparticles with an increase in the concentration of nanoparticles TiO_2 and their

Table 1. Elemental composition of the samples

Sample	C, at.%	F, at.%	O, at.%	K, at.%	Impurities, at.%
d-PVDF	61.49 ± 0.17	25.17 ± 0.50	13.07 ± 0.05	0.06 ± 0.01	0.31 ± 0.01
d-PVDF-TiO_2-0.5	62.43 ± 0.54	24.61 ± 0.56	12.68 ± 0.24	0.20 ± 0.55	0.08 ± 0.01
d-PVDF-TiO_2-1.0	59.09 ± 4.09	26.88 ± 4.90	13.30 ± 1.70	0.30 ± 0.44	0.42 ± 0.30
d-PVDF-TiO_2-5.0	63.55 ± 0.78	23.20 ± 1.52	13.04 ± 0.80	0.12 ± 0.02	0.09 ± 0.01
PVDF	49.69 ± 2.11	50.29 ± 2.09	–	–	–

sizes decrease as a result. For instance, the pore sizes range from 26 to 110 nm for the sample of d-PVDF-TiO_2-1.0, the surface concentration reaches $29.2\,\mu m^{-2}$, and the distance between them is 185 nm. The pore surface concentration is $13.1\,\mu m^{-1}$. For sample of d-PVDF-TiO_2-5.0, the pore sizes range from 27 to 82 nm, the surface concentration reaches $35.4\,\mu m^{-2}$, and the distance between them is 168 nm. The pore surface concentration is $4.1\,\mu m^{-1}$. Also, an increase in the concentration of TiO_2 nanoparticles results in the appearance of their agglomerates with sizes of the order of 200 nm.

Thus, the addition of TiO_2 nanoparticles increases the size of pores on the surface of the samples, but these pores are also filled with TiO_2 nanoparticles, which reduces the range of pore sizes on the surface of the samples.

3.2. Energy dispersive X-ray spectroscopy

Table 1 shows the elemental composition of the initial PVDF precursor obtained as a film, a dehydrohalogenated sample of d-PVDF and composites of d-PVDF-TiO_2 with a different mass fraction of TiO_2 (0.5, 1 and 5 %).

For the initial PVDF precursor, the ratio $C:F = 0.99 \pm 0.06$. In general, all samples contain less than 1.5 % of impurities (K, Na, Ca, Al, Si), the presence of which can be explained by incomplete lifting of KOH reagent or the presence of residual impurities. Dehydrohalogenated samples generally contain fewer F atoms compared to the PVDF precursor, and no significant changes in the phase ratio were observed with the addition of TiO_2 nanoparticles.

In addition, the dehydrohalogenated samples exhibit significant oxidation, at which the proportion of O atoms is 13 %. These results are consistent with the results in Ref. [15], which indicate that OH formation occurs during and after dehydrohalogenation under atmospheric conditions.

3.3. Infrared spectroscopy

Figure 3 shows the IR spectra of samples d-PVDF, d-PVDF-TiO_2-0.5, d-PVDF-TiO_2-1.0 and d-PVDF-TiO_2-5.0.

The absorption bands from 410 to 480 cm^{-1} are characteristic of the PVDF structure [16,17]. The frequency in the range from 850 to 1550 cm^{-1} corresponds to the lines

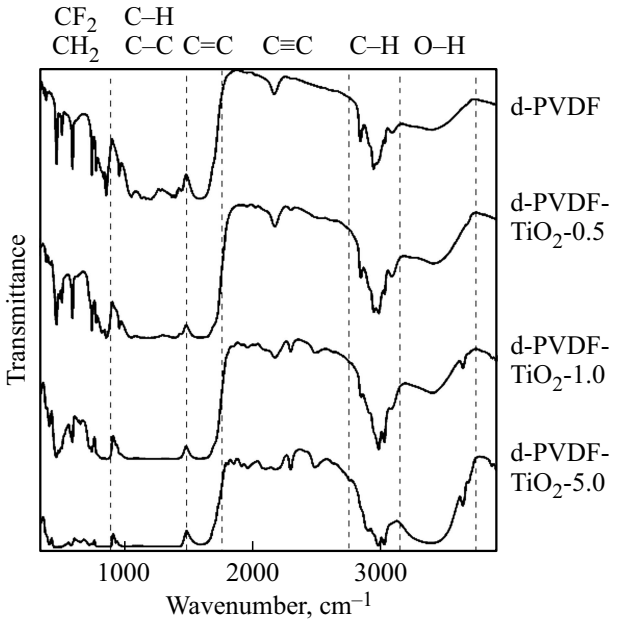

Figure 3. IR spectrum.

of various carbon, polymer, and polymer-like structures. A more detailed description of the lines within this area for the sample d-PVDF is presented in Ref. [4]. Most of the above-described lines broaden with an increase in the concentration of TiO_2 nanoparticles in the d-PVDF structure possibly due to an increase in the degree of material disordering in these structures. The lines at frequencies of 870 and 970 cm^{-1} correspond to the oscillations of C−H [18,19].

Also, the oscillations of C−H for bending are characterized by a frequency of 1390 cm^{-1}, which is superimposed by the oscillation of C−C for stretching [20].

The lines at frequencies of 1060 and 1210 cm^{-1} belong to the oscillations of groups C−C, C−O and C−O−C [18,21].

When nanoparticles TiO_2 are added, lines with maxima at 434 and 656 cm^{-1} appear in the spectrum [22]. Also, when nanoparticles are added, a line appears on the spectra at 511 cm^{-1}, which corresponds to the βphase of PVDF [16].

The line at a frequency of 1600 cm^{-1} corresponds to tension oscillations C=C [18]. The presence of this line

Table 2. Raman spectrum fitting parameters. The positions (k_{max}), half-widths at half-height (HWHM), and relative intensities (I_{rel}) of the lines are presented

	Line	k_{max}, cm^{-1}	HWHM, cm^{-1}	I_{rel}, %		Line	k_{max}, cm^{-1}	HWHM, cm^{-1}	I_{rel}, %
d-PVDF	C−C	1134.5	15.4	17.0	d-PVDF−TiO_2-1.0	C−C	1154.7	33.4	8.0
	C=C	1524.3	22.7	61.1		C=C	1543.4	43.2	58.7
	cis-C−C	1237.8	35.5	4.6		cis-C−C	1264.3	112.2	16.6
	cis-C−C	1376.3	20.0	6.3		cis-C−C	1448.0	14.9	1.2
	D	1321.5	32.7	6.4		D	1347.2	64.6	10.8
	G	1577.8	53.7	4.6		G	1601.0	36.7	4.8
d-PVDF-TiO_2-0.5	C−C	1153.2	29.1	7.7	d-PVDF-TiO_2-5.0	C−C	1161.0	31.4	7.0
	C=C	1543.9	47.5	66.9		C=C	1547.7	48.9	45.3
	cis-C−C	1251.3	84.1	14.0		cis-C−C	1283.9	53.7	9.3
	cis-C−C	1444.5	9.0	0.5		cis-C−C	1447.4	16.1	5
	D	1350.7	54.3	9.1		D	1380.3	36.8	7.9
	G	1603.8	28.2	1.8		G	1634.7	105.4	25.6

indicates that the PVDF material was not completely dehydrofluorinated during chemical treatment. As a result, an additional polyene component of the type $(-CH=CF-)_n$ is formed, which can participate as a separate fragment in the construction of the polyyne chain. The shape of this line remained constant for all samples, so we can talk about the same nature of incomplete dehydrohalogenation for all samples.

The absorption line at 2170 cm^{-1} is characterized by bond tension fluctuations of C≡C. This oscillation is typical for long polyyne chains [23]. It is also worth noting that this line is typical for structures with single triple bonds in the structure of the polymer chain [24]. Apparently, the structure under study is represented as a set of fragments of the polyene and polyyne type [25].

The frequency range of 2840 and 2950 cm^{-1} is associated with fluctuations of the aliphatic groups [26,27]. It can be concluded that the structure is represented in the form of long molecular chains. It is also worth noting the line at frequencies of 3390 and 3630 cm^{-1}, associated with OH groups, which is caused by the processes of oxidation and hydrogenation of the sample surface under atmospheric conditions [18,28].

With a change in the weight fraction of nanoparticles TiO_2 in the produced samples, a strong change in lines is observed in the frequency range from 1800 to 2700 cm^{-1}. Thus, there is an increase in the contribution of lines at the frequencies 1963, 2025 and 2300 cm^{-1}, which also appear in the spectra of the original d-PVDF, but having a low intensity [4]. The these lines appear most likely due to an increase in the degree of disorder of the initial precursor upon the introduction of TiO_2 nanoparticles. New lines appear in addition to the listed lines at 1814, 1919, 2083, 2106, 2216 cm^{-1} [29] related to the formation of linear fragments based on sp-hybridized carbon based on C≡C bonds. It is worth noting that the frequency region in the range of 2700−3200 cm^{-1} associated with tension oscillations of C−H bonds does not change, which indicates the preservation of the linear configuration of the molecular structure of the samples.

Thus, the following main features of the IR spectra can be defined:

1. A disordering of the general structure of dehydrohalogenated PVDF is observed [30] as wells as the appearance of an absorption line of nanoparticles TiO_2.

2. The appearance of chains based on polyyne and polyene fragments of various lengths in the structure of

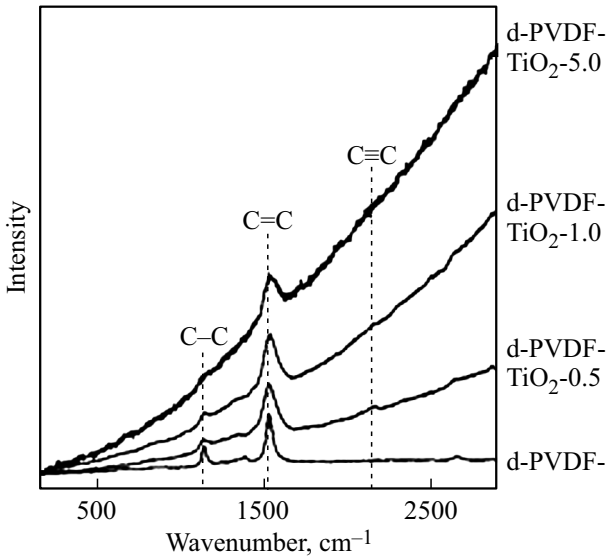

Figure 4. Raman spectrum with background.

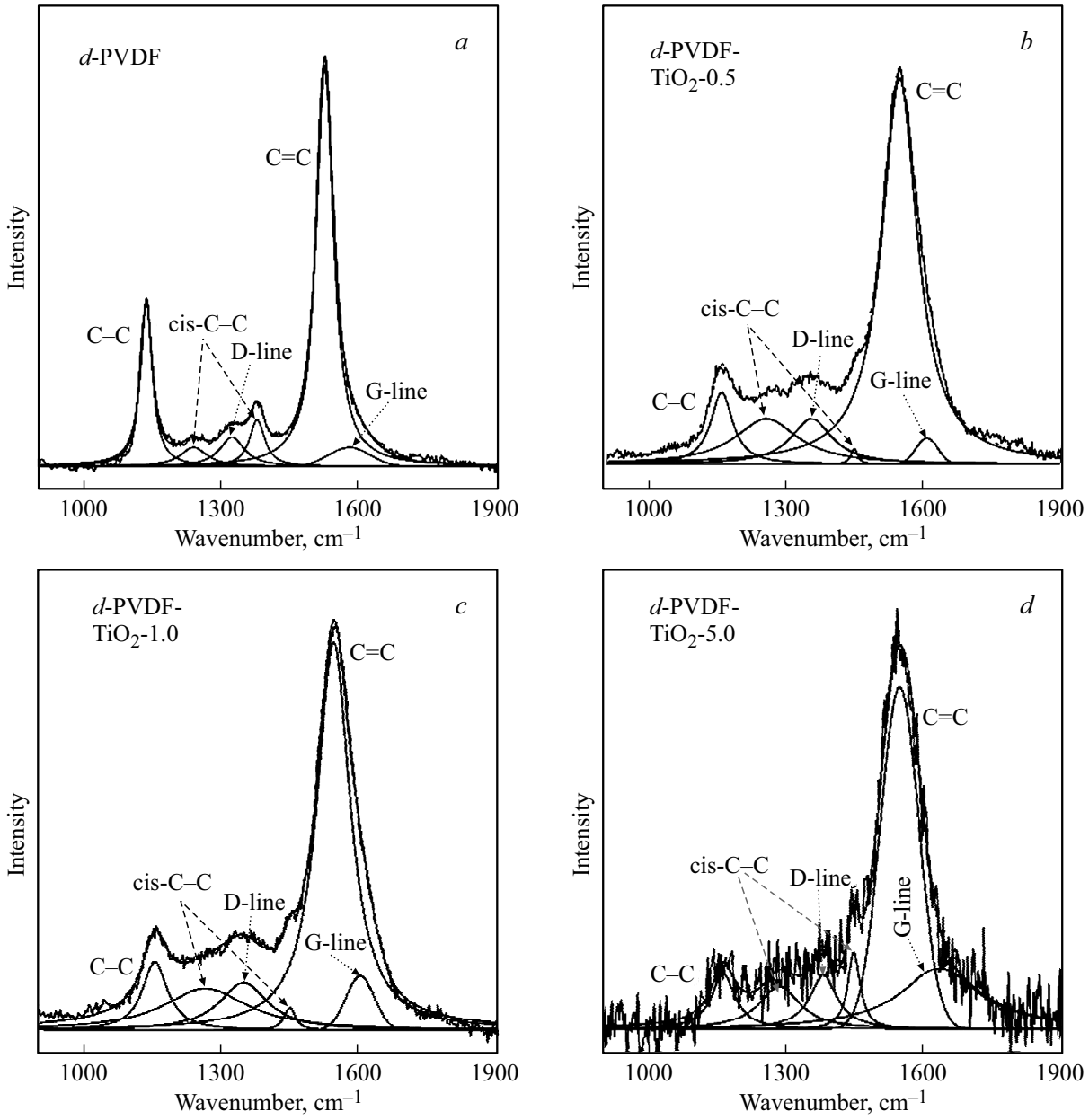

Figure 5. *a*) Raman spectra of d-PVDF, *b*) d-PVDF-TiO_2-0.5, *c*) d-PVDF-TiO_2-1.0, *d*) d-PVDF-TiO_2-5.0, approximated by Gauss−Lorentz components.

the samples, while maintaining the linear appearance of the molecular chains.

3.4. Raman spectroscopy

Figure 4 shows the Raman spectra of d-PVDF light and d-PVDF-TiO_2 composites with different mass fractions of TiO_2 nanoparticles. All the presented spectra were approximated by five Gauss−Lorentz components. The fitting parameters of the Raman spectra were estimated to analyze the changes in the structure of the material depending on the mass fraction of nanoparticles TiO_2 (Figure 5). The data is presented in Table 2.

The fitting was performed for the RS lines, the background of which was subtracted by the MagicPlot software package using the user-defined spline tool.

A number of features can be distinguished on the presented spectra. The peak in the frequency range 1130−1160 cm^{-1} [31] is associated with fluctuations C−C of the linear component in the sample structure. Also, the peak in the frequency range 1230−1260 cm^{-1} corresponds to the cis-isomeric structure C−C [32]. The frequency range 1340−1380 cm^{-1} is associated with the breathing mode of graphite rings, which is denoted as the D-line [33], and the peak at frequencies 1520−1550 cm^{-1} is associated with C=C-tensile vibrations in polymer chains [34]. The

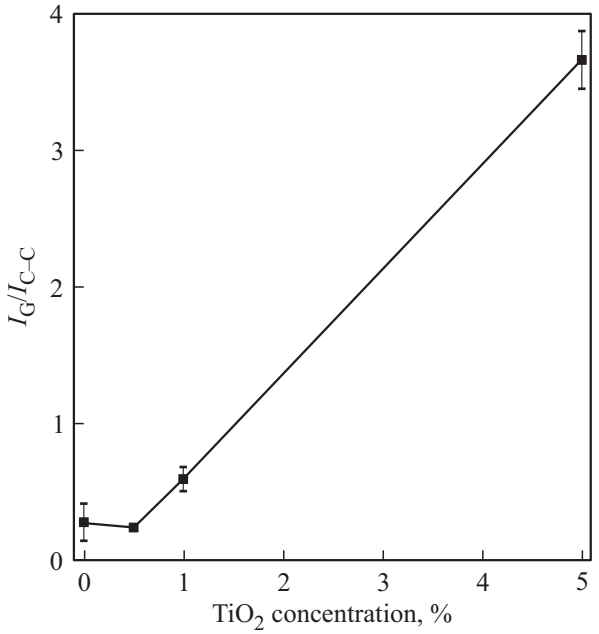

Figure 6. Dependence of the integral ratio of the G-line to the C=C communication line on the mass fraction of the nanoparticle content TiO_2.

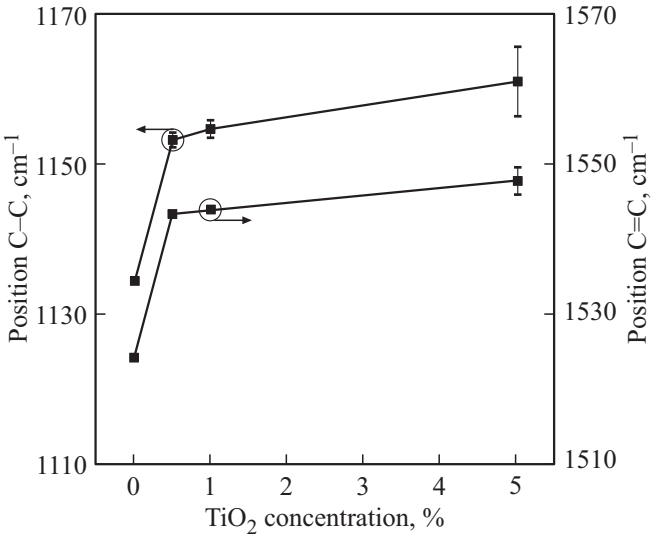

Figure 7. Dependence of the position of the Raman spectrum lines on the concentration of nanoparticles TiO_2.

frequency range $1580-1590\,cm^{-1}$ is associated with oscillations of the graphite-like component and is referred to in the literature as the G-line [35]. In combination, the D- and G-lines are responsible for the amorphous carbon component in the sample.

When nanoparticles TiO_2 are added to the sample, the proportion of the amorphous component increases, as well as a change in the chain structure (Figure 6).

When nanoparticles TiO_2 are added to the Raman spectra of the samples, there is a sharp shift of the lines associated with fluctuations C−C of the linear component and with fluctuations C=C on tension in polymer chains (Figure 7) to large wavenumbers. This behavior indicates the shortening of linear fragments and the formation of crosslinking with an increase in the concentration of nanoparticles TiO_2. Shortening and crosslinking of linear fragments may occur due to the formation of Ti−O−C bonds and a large number of defects in case of dehydrohalogenation of PVDF-TiO_2 film [36]. But starting from 0.5 %, the change in the position of the lines does not occur so sharply and corresponds to a linear growth.

Most likely, the presence of nanoparticles TiO_2 leads to disruption of the chain formation mechanism during dehydrohalogenation; also, most likely, nanoparticles serve as the initial centers of formation of new linear structures due to dehydrohalogenation. In addition, these structures can be localized near nanoparticles, forming an altered phase surrounding the nanoparticles, which, in turn, leads to an increase in the intensity of the overall luminescence background and shortening of linear fragments.

It is also worth noting that with an increase in the mass fraction of the content of TiO_2 nanoparticles in the d-PVDF-TiO_2 sample, not only a change in the phase ratio occurs, but also an increase in the overall luminescence background, which is apparently associated with an increase in the degree of disordering of the structure and formation of defects.

It is noteworthy that the bond line associated with polyyne chains and characterizing bond stretching fluctuations C≡C [37] was not observed for the d-PVDF at $2140-2170\,cm^{-1}$ sample. This behavior may be related to a luminescence peak that falls within a given frequency range [4]. In addition, the C≡C bond line may not be observed in the Raman spectra due to frequency selection rules, as a result of which the components of the polarization matrix do not change when the chains oscillate, as well as due to shortening the length of the chains, which leads to a decrease in the intensity of the raman signal [23]. A low-intensity peak is observed at 2147 cm^{-1} when nanoparticles TiO_2 are added. The addition of nanoparticles TiO_2 apparently leads to a violation of the selection rules for the C≡C bond line. This explanation is consistent with the results obtained using IR, where absorption lines are observed near $2147\,cm^{-1}$. The intensity of the line $2147\,cm^{-1}$ decreases with a further increase in the mass fraction of the content of TiO_2 nanoparticles in the d-PVDF film-TiO_2, which may be associated with a significant increase in the luminescence background of the samples and an increase in the degree of disordering of the structure.

Changes in the Raman spectra of light are the result of phase rearrangements in the samples and are not the result of the appearance of nanoparticle bonding lines in this region TiO_2, since the bond lines are in the region of low wavenumbers (less than $1000\,cm^{-1}$) [38].

When TiO_2 nanoparticles are added, there is a slight increase in the HWHM values for the C−C, C=C, cis-C−C

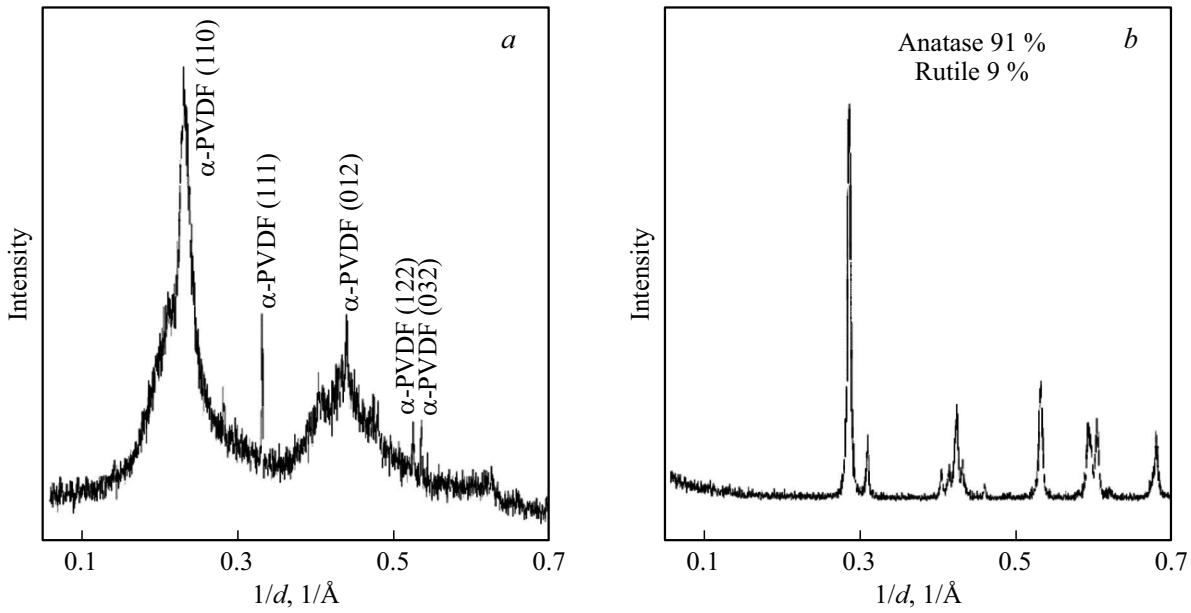

Figure 8. XRD for *a*) d-PVDF-TiO_2-0.5 and *b*) TiO_2.

and D-lines, which indicates disordering when nanoparticles are added. The position of the C−C and C=C bond lines shifts towards higher wavenumbers with an increase in the mass fraction of TiO_2 nanoparticles in the d-PVDF film, which indicates a shortening of polyene chains.

3.5. X-ray diffraction analysis (XRD)

Figure 8 shows typical diffraction patterns of samples of d-PVDF-TiO_2 and pure powder of nanoparticles TiO_2. The X-ray image of the nanoparticles TiO_2 consists of 11 relatively narrow peaks. The nanoparticles TiO_2 used in this study exist in two polymorphic structural modifications: anatase [39] and rutile [40]. Peaks that correspond to interplane distances 3.51 Å (101), 2.42 Å (103), 2.36 Å (004), 2.32 Å (112), 1.88 Å (200), 1.69 AA (105), 1.66 Å (211), 1.47 Å (204), determine anatase (91 %); peaks that correspond to interplane distances 3.23 Å (110), 2.48 Å (101), 2.19 Å (111), determine rutile (9 %). Thus, nanoparticles are mainly represented in the form of anatase in our study. The fitting of diffraction patterns with Gaussian lines, followed by an estimate of the phase fractions, was performed in the MagicPlot software package.

The diffraction patterns of samples containing TiO_2 nanoparticles practically do not differ from the diffraction pattern of d-PVDF, and it is not possible to isolate the phase corresponding to the nanoparticles in the samples. Figure 8 shows a X-ray diffraction pattern of the d-PVDF-TiO_2 sample. It consists of 8 lines. The peaks corresponding to the interplane distances 3.02 Å (111), 1.91 Å (122), 1.87 Å (032) determine the α-modification of PVDF, which remained after chemical treatment of the films. The peaks corresponding to the interplane distances 4.76, 4.37, 2.46, 2.28, and 2.10 Å characterize two phases: α-modification of PVDF [41] for planes (020), (110), (200), (012), (102), as well as the phase characteristic of disordered carbon chains [42]. The observation of PVDF crystallites in the structure of the samples indicates the residual material of the initial precursor. Wider peaks with interplane distances of 7.3, 4.1 and 2.3 Å are also observed on diffraction patterns. These positions of the diffraction maxima correspond to the polymer and polyene components in the structure of the material [15]. The d-PVDF samples are characterized by interplane distances of 4−5 Å [43], which corresponds to the presence of *sp*-carbon structures.

3.6. Sensory properties

Figure 9 shows the dependence of $\Delta\sigma/\sigma_0$ on the mass fraction of the content of nanoparticles TiO_2; at the same time, the concentrations of interacting gases were constant. The concentration was 30 kppm for ammonium hydroxide, ethanol, and acetone. Ammonium hydroxide was chosen as the „source“ of NH_3, because only a small number of particles form $HN_4^+ + OH^-$ ions in ammonium hydroxide, and mainly NH_3 is found as a dissolved gas in a liquid $HN_3 + H_2O$ [44].

The electrical conductivity of the d-PVDF sample increases when interacting with gases. This effect, which is due to charge transfer between the adsorbed gas and the highest occupied molecular orbital (HOMO) or the lowest unoccupied molecular orbital (LUMO) of the sample molecules, was considered in Ref. [4]. From this it can be concluded that the d-PVDF sample is a *n*-type semiconductor, as in Refs. [4,7], because the conductivity of the sample increases in case of interaction with donor molecules such as NH_3, $NH_3 + H_2O$, C_2H_5OH.

The addition of PVDF nanoparticles TiO_2 to the d- sample resulted in a significant increase in the response of $\Delta\sigma/\sigma_0$

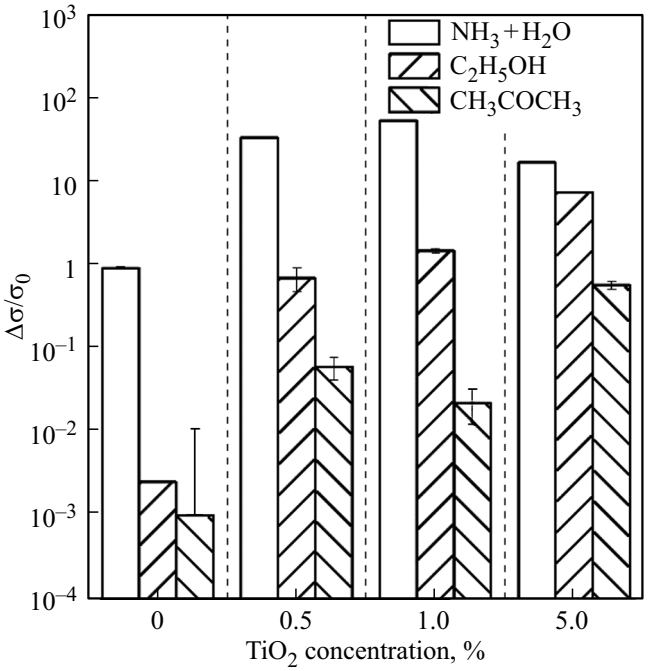

Figure 9. Dependence of the relative change in electrical conductivity on the mass fraction of nanoparticles TiO_2 for NH_3+H_2O, C_2H_5OH, CH_3COCH_3.

to NH_3+H_2O, C_2H_5OH, CH_3COCH_3. This effect may be associated with an increase in pore size when adding TiO_2 nanoparticles in the amount of 0.5 % of total weight. It was shown in Sec. 3.1 that pore sizes significantly increase on the surface of the sample d-PVDF-TiO_2-0.5, compared with the pore sizes of the original d-PVDF sample. An increase in pore size leads to an increase in the surface area on which the process of adsorption of gas molecules is possible. This, in turn, leads to an increase in the number of charge exchange processes between the adsorbed molecule and the sample, resulting in an increased response to vapors of substances [45]. In addition, based on the results of studies of IR spectroscopy and Raman spectroscopy of light, it can be concluded that with an increase in the concentration of TiO_2, phase changes occur in the composition of the sample, which can also contribute to an increase in the response of $\Delta\sigma/\sigma_0$ to vapors of substances [46]. Also, the increase in the response of $\Delta\sigma/\sigma_0$ to CH_3COCH_3 pairs can be influenced by the TiO_2 nanoparticles themselves, since the nanoparticles themselves are highly sensitive to CH_3COCH_3 [47].

An increase in the mass fraction of the content of TiO_2 nanoparticles in films to 1.0 % leads to a relatively small increase in the response to NH_3+H_2O, C_2H_5OH and a slight decrease in response to CH_3COCH_3 pairs. As it was seen from the results of the study in Sec. 3.1, an increase in the mass fraction of the content of nanoparticles TiO_2 to 1.0 % of the total mass leads to a decrease in the range of pore sizes on the sample surface and, consequently, to a decrease in the surface area for the adsorption of gas molecules. Therefore, this change does not contribute to an increased response to substance vapors. The influence of the phase composition on the response value $\Delta\sigma/\sigma_0$ is more likely [46]. According to the results of research in the section of IR spectroscopy, it was shown that the addition of nanoparticles to films in the amount of 1.0 % of the total mass leads to significant changes in the phase composition of the sample, which is reflected in changes in the relative intensities of the initial communication lines, as well as in the appearance of new communication lines.

At the maximum mass fraction of the TiO_2 nanoparticles (5.0 % of total weight) the value of response $\Delta\sigma/\sigma_0$ to NH_3+H_2O pairs decreases and it increases to C_2H_5OH, CH_3COCH_3 pairs. This phenomenon can be explained by the fact that an increase in the mass fraction of the content of nanoparticles TiO_2, which leads to clogging of pores on the surface, significantly reduces the surface area for adsorption of molecules. As a result, it is possible to reduce the response value for pairs, but this value is still greater than the response value for the original sample. This may be attributable to the fact that the value of the response $\Delta\sigma/\sigma_0$ to NH_3+H_2O pairs is influenced by TiO_2 nanoparticles, as well as new phases in the film composition. However, the responses to the C_2H_5OH, CH_3COCH_3 pairs did not decrease, but rather increased. Apparently, the contribution of the phase composition change was more significant for the response of $\Delta\sigma/\sigma_0$ to C_2H_5OH pairs. Basically, the behavior of change of the response of $\Delta\sigma/\sigma_0$ to CH_3COCH_3 pairs is determined by the presence of TiO_2 nanoparticles in the film, since, as already mentioned, nanoparticles are highly sensitive to CH_3COCH_3 pairs [47].

Figure 10 shows the typical dynamics of $\Delta\sigma/\sigma_0$ at one ethanol concentration as a function of time for four samples

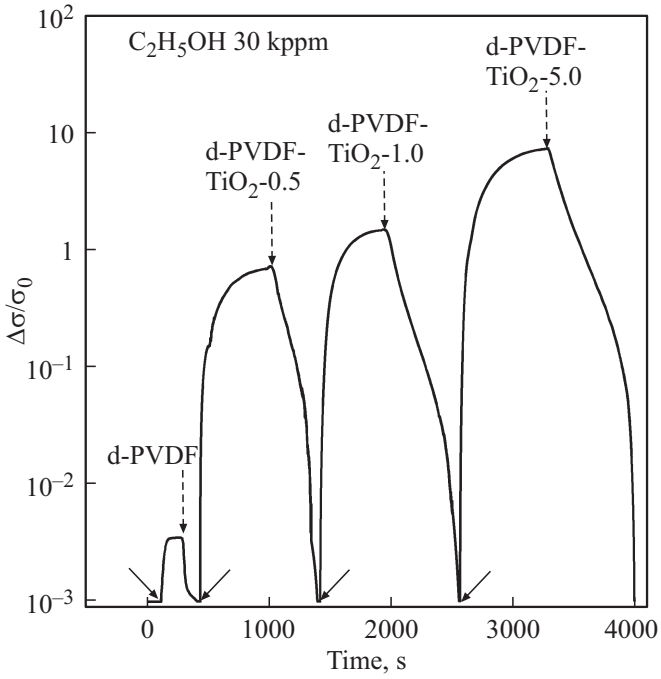

Figure 10. Time dependence of relative changes in electrical conductivity for different samples (d-PVDF, d-PVDF-TiO_2-0.5, d-PVDF-TiO_2-1.0, d-PVDF-TiO_2-5.0) at 30 kppm of ethanol.

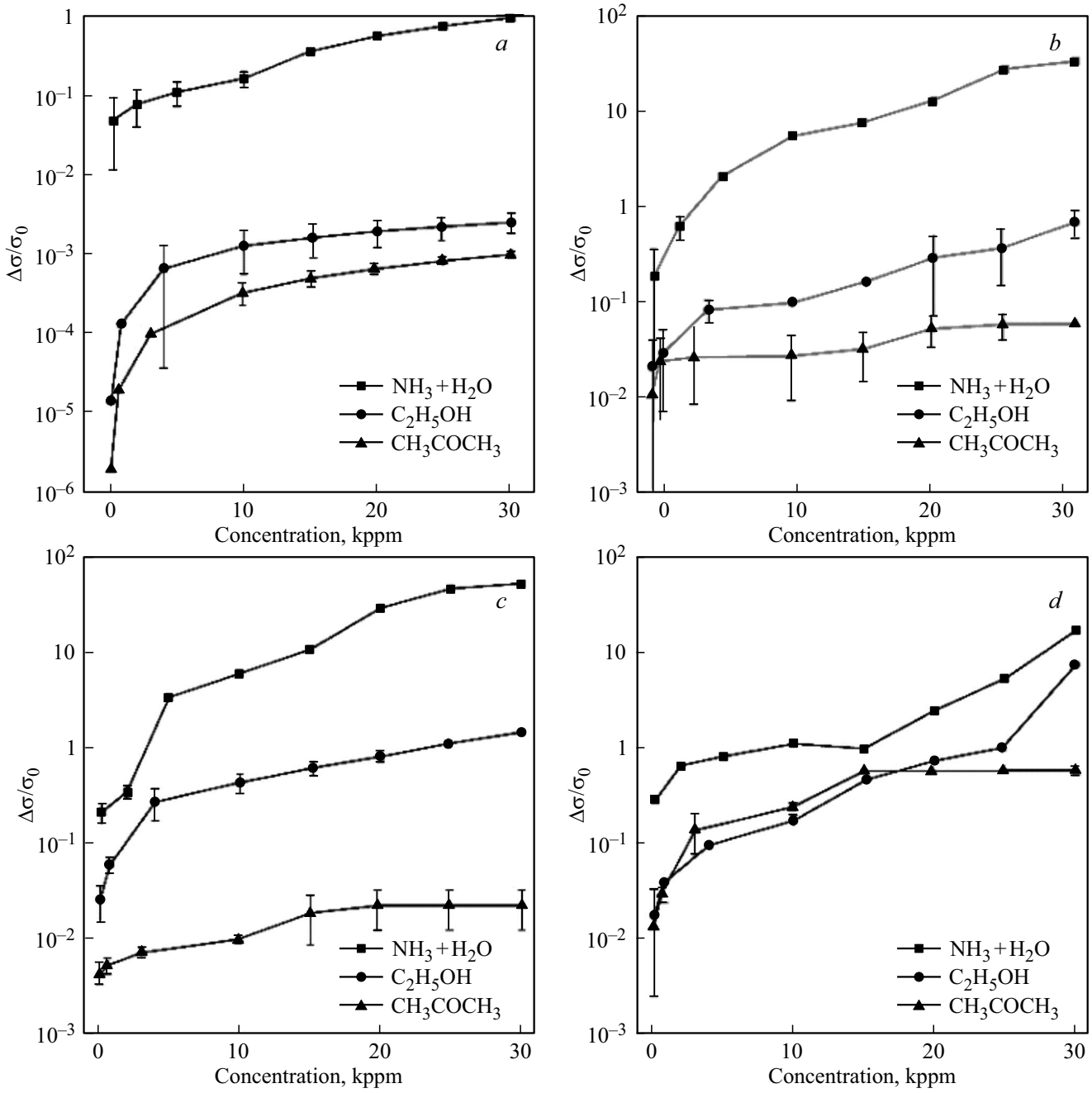

Figure 11. Dependence of the relative change in electrical conductivity on the concentration of gas molecules for *a*) d-PVDF, *b*) d-PVDF-TiO_2-0.5, *c*) d-PVDF-TiO_2-1.0, *d*) d-PVDF-TiO_2-5.0.

with different concentrations of nanoparticles TiO_2. The beginning of the increase (solid arrows) of the value $\Delta\sigma/\sigma_0$ indicates the moment of gas supply, and the beginning of the decrease (dotted arrows) indicates the time of closing of the gas supply. When considering the reaction and relaxation times for ethanol vapors, the values of these times increase with an increase in the mass fraction of the content of nanoparticles TiO_2. The reaction time to ethanol vapor is 0.8 min for sample of d-PVDF, 6.4 min for d-PVDF-TiO_2-0.5, the reaction time to ethanol vapor for d-PVDF-TiO_2-1.0 is 6 min, reaction time to ethanol vapor for d-PVDF-TiO_2-5.0 is 8.65 min. The time of relaxation to ethanol vapor is 0.7 min for sample of d-PVDF, 4 min for d-PVDF-TiO_2-0.5, 4.7 min for d-PVDF-TiO_2-1.0, 5.8 min for d-PVDF-TiO_2-5.0. However, when considering the reaction and relaxation time to ammonium hydroxide vapor (30 kppm), the value of these times changes nonmonotonously with an increase in the mass fraction of the content of nanoparticles TiO_2. The reaction time to ammonium hydroxide vapor is 2.8 min for sample of d-PVDF, 11.2 min for d-PVDF-TiO_2-0.5, 11.2 min for d-PVDF-TiO_2-1.0, 5.7 min for d-PVDF-TiO_2-5.0. The relaxation time for ammonium hydroxide vapors is 1.5 min

for sample of d-PVDF, 5.4 min for d-PVDF-TiO_2-0.5, 5.2 min for d-PVDF-TiO_2-1.0, 6.4 min for d-PVDF-TiO_2-5.0. The obtained reaction and relaxation times of these materials to ammonium hydroxide vapor turned out to be longer than reaction and relaxation times of nanotubes [48]. Acetone vapor reaction time is 2.9 min for sample of d-PVDF-TiO_2-0.5, 3.7 min for d-PVDF-TiO_2-1.0, 8.3 min for d-PVDF-TiO_2-5.0. Acetone vapor relaxation time is 1.0 min for the sample of d-PVDF-TiO_2-0.5, 2.2 min for d-PVDF-TiO_2-1.0, 4.95 min for d-PVDF-TiO_2-5.0.

Figure 11 shows the dependence of $\Delta\sigma/\sigma_0$ on the vapor concentration of ammonium hydroxide, ethanol, and acetone for four samples. These dependences are Langmuir adsorption isotherms, which demonstrate a gradual decrease in the slope of the corresponding curves at high concentrations of gases [49]. A noticeable saturation was observed for acetone vapors. Saturation with ammonium hydroxide vapors is apparently observed at concentrations exceeding those used in the described experiments.

The selectivity of the samples to vapors is shown in Figure 9. The concentration of ammonium hydroxide, ethanol and acetone is 30 kppm. For the sample d-PVDF, the response ratio for different pairs is $\Delta\sigma(NH_3{+}H_2O)/\Delta\sigma(C_2H_5OH) = 363$ and $\Delta\sigma(NH_3{+}H_2O)/\Delta\sigma(CH_3COCH_3) = 916$. When TiO_2 nanoparticles are added, the selectivity for ammonium hydroxide vapor decreases. So, for 0.5% of the nanoparticles TiO_2, the response ratios were

$$\Delta\sigma(NH_3 + H_2O)/\Delta\sigma(C_2H_5OH) = 48$$

$$\text{and } \Delta\sigma(NH_3 + H_2O)/\Delta\sigma(CH_3COCH_3) = 555,$$

$$\text{for } 1.0\% - \Delta\sigma(NH_3 + H_2O)/\Delta\sigma(C_2H_5OH) = 39$$

$$\text{and } \Delta\sigma(NH_3 + H_2O)/\Delta\sigma(CH_3COCH_3) = 2377,$$

$$\text{for } 5.0\% - \Delta\sigma(NH_3 + H_2O)/\Delta\sigma(C_2H_5OH) = 2$$

$$\text{and } \Delta\sigma(NH_3 + H_2O)/\Delta\sigma(CH_3COCH_3) = 29.$$

4. Conclusion

Carbon structures based on polyene-polyyne, consisting of chains with polyene (sp^2-carbon polymer) and polyyne (sp-carbon polymer) fragments, with the addition of TiO_2 nanoparticles, have been studied. The studied material was created by drop-casting of PVDF-TiO_2 film and subsequent KOH treatment at room temperature. The addition of nanoparticles TiO_2 leads to a change in the phase composition, as well as the morphology of the film surface.

A relatively selective response to $NH_3{+}H_2O$ vapors is observed for the sample of d-PVDF at room temperature: $\Delta\sigma(NH_3{+}H_2O)/\Delta\sigma(C_2H_5OH) = 363$ and $\Delta\sigma(NH_3{+}H_2O)/\Delta\sigma(CH_3COCH_3) = 916$. The addition of TiO_2 nanoparticles leads to a decrease in the selective response to $NH_3{+}H_2O$ pairs. Moreover, there is an optimal mass fraction of the content of TiO_2 nanoparticles, at which the response to $NH_3{+}H_2O$ pairs is maximal. An increase in the mass fraction of the content of TiO_2 nanoparticles leads to an increase in sensitivity to ethanol and acetone vapors.

The results of the conducted study have shown the prospects of using the obtained carbon material to create efficient new-generation gas sensors, the ability to increase their sensitivity in the analysis of multicomponent gas media, and adjust the sensory properties of the material necessary to solve the required tasks.

Acknowledgment

We would like to thank T.V. Filippova for conducting XRD measurements.

Conflict of interest

The authors declare that they have no conflict of interest.

References

[1] Z. Wang, L. Zhu, S. Sun, J. Wang, W. Yan. Chemosensors **9**, *8*, 198 (2021).
[2] N. Musayeva, H. Khalilova, B. Izzatov, G. Trevisi, S. Ahmadova, M. Alizada. C **9**, *1*, 25 (2023).
[3] V. Chaudhary, A. Gautam, Y.K. Mishra, A. Kaushik. Nanomater. **11**, *10*, 2496 (2021).
[4] I.A. Zavidovskiy, O.A. Streletskiy, I.F. Nuriahmetov, O.Y. Nishchak, N.F. Savchenko, A.A. Tatarintsev, A.V. Pavlikov. J. Compos. Sci. **7**, *4*, 156 (2023).
[5] O.A. Streletskiy, I.A. Zavidovskiy, I.F. Nuriahmetov, O.Y. Nishchak, A.V. Pavlikov, N.F. Savchenko. C **9**, *3*, 82 (2023).
[6] D.A. Giannakoudakis, T.J. Bandosz. ACS Appl. Mater. Interfaces **12**, *13*, 14678 (2020).
[7] O.A. Streletskiy, I.A. Zavidovskiy, I.F. Nuriahmetov, A.A. Khaidarov, A.V. Pavlikov, K.F. Minnebaev. J. Compos. Sci. **7**, *7*, 264 (2023).
[8] B. Pan, J. Xiao, J. Li, P. Liu, C. Wang, G. Yang. Sci. Adv. **1**, *9*, e1500857 (2015).
[9] A.L. Eaton, M. Fielder, A.K. Nair. MRS Bull. **47**, *10*, 1001 (2022).
[10] Z. Zanolli, G. Onida, J.-C. Charlier. ACS Nano. **4**, *9*, 5174 (2010).
[11] M. Wang, S. Lin. Sci. Rep. **5**, *1*, 18122 (2015).
[12] Y. Prazdnikov. J. Modern Phys. **6**, *4*, 396 (2015).
[13] E.A. Nunes Simonetti, T. Cardoso de Oliveira, E. do Carmo Machado, A.A. Coutinho Silva, A. Silva dos Santos, L. de Simone Cividanes. Ceram. Int. **47**, *13*, 17844 (2021).
[14] A.J. Dias, T.J. McCarthy. J. Polym. Sci. Polym. Chem. Ed. **23**, *4*, 1057 (1985).
[15] V.E. Zhivulin, L.A. Pesin, E.A. Belenkov, V.A. Greshnyakov, N. Zlobina, M. Brzhezinskaya. Polym. Degrad. Stab. **172**, 109059 (2020).
[16] X. Cai, T. Lei, D. Sun, L. Lin. RSC Adv. **7**, *25*, 15382 (2017).
[17] Y Bormashenko, R. Pogreb, O. Stanevsky, E. Bormashenko. Polym. Test. **23**, *7*, 791 (2004).
[18] V. Tucureanu, A. Matei, A.M. Avram. Crit. Rev. Anal. Chem. **46**, *6*, 502 (2016).

[19] K. Prabakaran, S. Mohanty, S.K. Nayak. J. Solid State Electrochem. **19**, *8*, 2465 (2015).
[20] N. Dahmouchéne, S. Coppée, M. Voué, J. De Coninck. Physica Status Solidi C **5**, *5*, 1210 (2008).
[21] E. Pamuła, M. Błazewicz, C. Paluszkiewicz, P. Dobrzynski. J. Mol. Struct. **596**, *1–3*, 69 (2001).
[22] N. Lagopati, E.P. Tsilibary, P. Falaras, P. Papazafiri, E.A. Pavlatou, E. Kotsopoulou, P. Kitsiou. Int. J. Nanomed. **9**, *1*, 3219 (2014).
[23] A. Lucotti, M. Tommasini, D. Fazzi, M. Del Zoppo, W.A. Chalifoux, M.J. Ferguson, G. Zerbi, R.R. Tykwinski. J. Am. Chem. Soc. **131**, *12*, 4239 (2009).
[24] T.X. Leong, B.K. Collins, S.D. Baksi, R.T. Mackin, A. Sribnyi, A.L. Burin, J.A. Gladysz, I.V. Rubtsov. J. Phys. Chem. A **126**, *30*, 4915 (2022).
[25] V.E. Zhivulin, V.M. Chernov, A.A. Osipov, M.V. Shtenberg, S.E. Evsyukov, L.A. Pesin. Phys. Solid State **59**, *7*, 1414 (2017).
[26] C. Ehrendorfer, H. Neugebauer, A. Neckel, P. Bäuerle. Synth. Met. **55**, *1*, 493 (1993).
[27] L. Guo, S. Wu, F. Zeng, J. Zhao. Eur. Polym. J. **42**, *7*, 1670 (2006).
[28] O.A. Streletskiy, O.Y. Nishchak, I.A. Zavidovskiy, K.I. Maslakov, A.V. Pavlikov. Thin Solid Films **739**, 138993 (2021).
[29] F. Hu, C. Zeng, R. Long, Y. Miao, L. Wei, Q. Xu, W. Min. Nature Methods **15**, *3*, 194 (2018).
[30] A. Ujcic, M. Nevoralova, J. Dybal, A. Zhigunov, J. Kredatusova, S. Krejcikova, I. Fortelny, M. Slouf. Front. Mater. **6**, 284 (2019).
[31] B.H. Stuart. Vib. Spectrosc. **10**, *2*, 79 (1996).
[32] L. Palomo, R. Rodríguez, S. Medina, E. Quiñoá, J. Casado, F. Freire; F.J. Ramírez. Angew. Chem. **132**, *23*, 9165 (2020).
[33] O. Streletskiy, E. Perevedentseva, I. Zavidovskiy, A. Karmenyan, V. Sychev, V. Sadykova, A. Kuvarina, C.-L. Cheng. Magnetochem. **8**, *12*, 171 (2022).
[34] L.F. Maia, V.E. De Oliveira, H.G.M. Edwards, L.F.C. De Oliveira. Chem. Phys. Chem. **22**, *3*, 231 (2021).
[35] P. Sharma, G. Sharma, R. Punia. Appl. Phys. A **127**, *5*, 319 (2021).
[36] A. Safri, A.J. Fletcher. Gels **9**, *6*, 468 (2023).
[37] O.A. Streletskiy, I.A. Zavidovskiy, O.Yu. Nischak, A.V. Pavlikov. Thin Solid Films **671**, 31 (2019).
[38] K.M. Lee, C.F. Kait, J.W. Lim, G.B. Teh. Proceed. 6th Int. Conf. Fundamental. Appl. Sci. 85 (2020).
[39] S.S. El-Deen, A.M. Hashem, A.E. Abdel Ghany, S. Indris, H. Ehrenberg, A. Mauger, C.M. Julien. Ionics **24**, *10*, 2925 (2018).
[40] S. Kityakarn, A. Worayingyong, A. Suramitr, M.F. Smith. Mater. Chem. Phys. **139**, *2–3*, 543 (2013).
[41] B.A. Newman, C.H. Yoon, K.D. Pae, J.I. Scheinbeim. J. Appl. Phys. **50**, *10*, 6095 (1979).
[42] O.A. Streletskiy, I.A. Zavidovskiy, O.Y. Nischak, A.A. Khaidarov, N.F. Savchenko, A.V. Pavlikov. JETP **135**, *6*, 844 (2022).
[43] Yu.P. Kudryavtsev, S.E. Evsyukov, V.G. Babaev, M.B. Guseva, V.V. Khvostov, L.M. Krechko. Carbon **30**, *2*, 213 (1992).
[44] W. Lang, T.M. Blöck, R. Zander. Clinica Chimica Acta **273**, *1*, 43 (1998).
[45] G.-G. Lee, S.-J.L. Kang. Sensors. Actuators B Chemical **107**, *1*, 392 (2005).
[46] M. Wang, T. Hou, Z. Shen, X. Zhao. Sensors. Actuators B: Chemical **292**, 171 (2019).
[47] N. Jayasaranya, R. Ezhil Pavai, L. Balu, C. Manoharan. J. Mater Sci.: Mater. Electronics **35**, *3*, 208 (2024).
[48] T. Pandhi, A. Chandnani, H. Subbaraman, D. Estrada. Sensors **20**, *19*, 5642 (2020).
[49] S. Gomri, J.-L. Seguin, J. Guerin, K. Aguir. Sensors. Actuators B Chemical **114**, *1*, 451 (2006).

Translated by A.Akhtyamov